

Synthesis of Hierarchically Porous Zeolite Composites with Enhanced Catalytic Activity: Effect of Different Long-Chain Structure Directing Agents

He Ding,^{†,§,#} Yixiao Zhang,^{†,§,#} Zixing Xiao,^{†,§} Jingshuang Zhang,^{†,§} Peng Bai,^{†,§} Najun Li,[‡] and Xianghai Guo^{*,†,§}

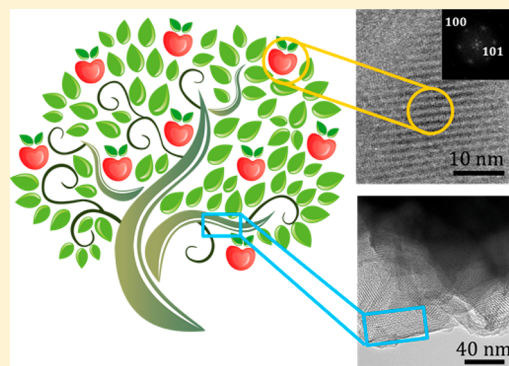
[†]Department of Pharmaceutical Engineering, School of Chemical Engineering and Technology, Tianjin University, Tianjin 300350, China

[§]Key Laboratory of Systems Bioengineering, Ministry of Education, Tianjin 300350, China

[‡]College of Chemistry, Chemical Engineering and Materials Science, and Collaborative Innovation Center of Suzhou Nano Science and Technology, Soochow University, Suzhou, Jiangsu 215123, China

Supporting Information

ABSTRACT: A two-section temperature strategy was employed to achieve microporous composites with five kinds of long-chain alkyl quaternary ammonium salts as single template. Zeolites with an ordered two-dimensional hexagonal mesopore and crystallized MFI domain were successfully obtained. Gemini quaternary ammonium salt surfactants C₁₈N₂ and C₂₂N₂ are effective in directing the structure of MCM-41 than CTAB at 100 °C and will transform to lamellar MFI structures at 150 °C gradually. While single quaternary ammonium salts C₁₈N and C₂₂N direct lamellar M41s at 100 °C and transform to mesoporous structure at a higher temperature of 150 °C, it is possible to get a composite of microporous and mesoporous material with a surface area as high as 1046 m² g⁻¹. Catalytic performance of typical hierarchical zeolites was evaluated by Claisen-Schmidt condensation of bulky reactants. The excellent conversion suggested the synergy effects of improved large molecule diffusion in mesopores and highly separated MFI domains as catalytic centers in the hierarchical zeolites, which can be explained by an apple-tree model.



1. INTRODUCTION

MCM-41 (a member of the M41s family), a typical mesoporous silica-based materials discovered by researchers at Mobil Oil Company^{1,2} in the 1990s, attracted remarkable attention in various applications.^{2,3} Due to the one-dimensional regular pore diameter (range of 1.5–6.5 nm), high specific surface area, large pore volume, and high density of surface silanols,⁴ MCM-41 manifested itself as a very promising candidate in catalysis, adsorption, and the separation process. However, the relatively poor structural stability (compared with zeolites) was still a bottleneck for the further applications in petroleum refining and fine chemical industry so far.^{5,6} A few strategies have been developed to enhance the stability, such as surface modification,^{7–9} salt treatment,¹⁰ grafting method,¹¹ and crystallization of amorphous mesoporous wall.¹²

Through a dual-template method with multisteps, micro- and meso-porous composite materials were synthesized with improved hydrothermal stability, such as silicalite-1/MCM-41,^{13,14} β /MCM-41,^{15,16} and Y/MCM-41.¹⁷ Yang developed a facile route to prepare silica-based bimodal micro/mesoporous hybrids with a mixed silica source.¹⁸ A seed crystallization method has also made significant advances in improving the

hydrothermal stability of mesoporous structures.^{19–21} Many ordered mesoporous materials were tried to form crystallized pore wall, but MCM-41 stayed as the focus in spite of intrinsic limitations of pore wall thickness.

Recently, Ryoo had developed a selective approach to synthesize hierarchically unilamellar and multilamellar silicalite-1 zeolite, in which a series of dual-function surfactants with multiammonium groups were served as sole structure-directing agents.^{22,23} Although a soft template strategy demonstrated the feasibility of directing mesoporous zeolite, the long-range ordering of mesoporous structures was still restricted due to the intrinsic trade-off between the zeolite and mesoporous structure. Aware of similarity of multiammonium surfactants developed by Ryoo to CTAB, we envisaged that these structure-directing agents might also generate mesoporous structure of MCM-41. With a big head in the ammonium end, an increased pore wall thickness is expected, which could possibly overcome the crystallization barrier of MCM-41.

Received: November 27, 2017

Revised: January 24, 2018

Published: February 15, 2018

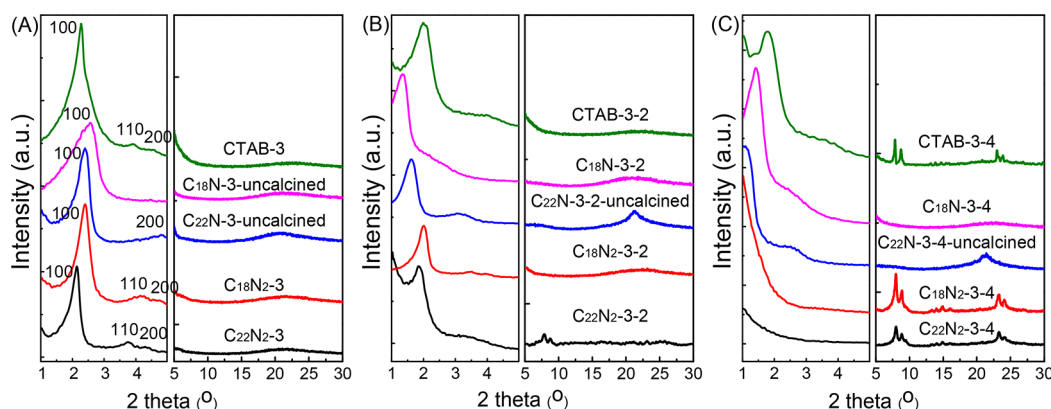


Figure 1. XRD patterns of samples reacting 3 d at 100 °C (A); 3 d at 100 °C and then 2 d (B) or 4 d (C) at 150 °C.

Along this reflection, we developed a simple synthetic system of silicalite-1/MCM-41 composite with single long-chain surfactant. Hierarchical composites with highly scattered MFI structure among the unoriented mesoporous structures provided a possible strategy for overcoming the diffusion limit of bulk reactants. In this contribution, a one-pot temperature-gradient strategy with only one surfactant was applied to obtain hierarchical MFI/MCM-41 composites. Some dual-quaternary ammonium salts were proven to be able to direct highly separated MFI domains in mesopores. A classical reaction of bulk molecules was performed to illustrate the excellent catalytic ability of this micro/mesoporous composite. Findings from this work have great potential to be developed as a platform technique for preparation of a variety of micro/mesoporous composites and bring new opportunities for the syntheses of growth-controllable micro/mesoporous zeolite materials with long-range order for advanced catalysis applications.

2. EXPERIMENTAL SECTION

Materials. Hexadecyl trimethylammonium bromide (CTAB, 99%) was purchased from Aladdin Industrial Corporation. Tetraethyl orthosilicate (TEOS, 96%), sodium hydroxide (2.0 M in water), 1-bromodocosane ($C_{22}H_{45}Br$, > 98%), 1-bromooctadecane ($C_{18}H_{37}Br$, > 97%), 1-bromohexane ($C_6H_{13}Br$, > 98%), and N,N,N',N' -tetramethyl-1,6-diaminohexane ($C_{10}H_{24}N_2$, > 98%) were purchased from Tokyo Chemical Industry Co., Ltd. Aluminum sulfate octadecahydrate ($Al_2(SO_4)_3 \cdot 18H_2O$), 2-hydroxyacetophenone ($C_8H_8O_2$, 98%), and benzaldehyde (C_6H_5CHO , GCS) were purchased from Aladdin Industrial Corporation. Ammonium acetate and (CH_3COONH_4) (1.0 M) were purchased from Macklin Biochemical Co., Ltd. Ethanol absolute (AR), acetonitrile (AR), methanol (AR), diethyl ether (AR), toluene (AR), chloroform (AR), and deionized water were purchased from Tianjin University Kewei LLC.

Preparation of Structure-Directing Agents (OSDA). The process of synthesis $[C_{22}H_{45}-N^+(CH_3)_2-C_6H_{12}-N^+(CH_3)_2-C_6H_{13}]Br_2^-$ ($C_{22}N_2$) was developed by Ryoo.²² In brief, 1-bromodocosane and N,N,N',N' -tetramethyl-1,6-diaminohexane were used for synthesis $[C_{22}H_{45}-N^+(CH_3)_2-C_6H_{12}-N(CH_3)_2]Br^-$ ($C_{22}N$), which formed $C_{22}N_2$ by reacting further with 1-bromohexane. $[C_{18}H_{37}-N^+(CH_3)_2-C_6H_{12}-N(CH_3)_2]Br^-$ ($C_{18}N$) and $[C_{18}H_{37}-N^+(CH_3)_2-C_6H_{12}-N^+(CH_3)_2-C_6H_{13}]Br_2^-$ ($C_{18}N_2$) was synthesized by a similar route using 1-bromooctadecane as raw material. The details are in Supporting Information.

Preparation of MCM-41. The samples were synthesized according to Huo's procedures^{24,25} with a synthetic mixture of 1 OSDA (Organic Structure Directing Agent):8.31 SiO_2 :3.36 $NaOH$:1054 H_2O . Five kinds of OSDAs were used, including hexadecyl trimethylammonium bromide (CTAB), $[C_{22}H_{45}-$

$N^+(CH_3)_2-C_6H_{12}-N(CH_3)_2]Br^-$ ($C_{22}N$), $[C_{22}H_{45}-N^+(CH_3)_2-C_6H_{12}-N^+(CH_3)_2-C_6H_{13}]Br_2^-$ ($C_{22}N_2$), $[C_{18}H_{37}-N^+(CH_3)_2-C_6H_{12}-N(CH_3)_2]Br^-$ ($C_{18}N$), and $[C_{18}H_{37}-N^+(CH_3)_2-C_6H_{12}-N^+(CH_3)_2-C_6H_{13}]Br_2^-$ ($C_{18}N_2$). As reported in the literature, if given different conditions, the products will transform between MCM-41, lamellar M41s, and ZSM-5.^{24,26} Li reported that MCM-41/ZSM-5 composites could be prepared using a dual template method through a process of two-step crystallization.¹⁴ Our strategy is that MCM-41 like structure was obtained by single template at a lower temperature and then the temperature was raised in the hope of further crystallization. The hydrothermal synthesis was performed under three different conditions: (1) 3 d at 100 °C; (2) 3 d at 100 °C, then 2 d at 150 °C; (3) 3 d at 100 °C, then 4 d at 150 °C. Then the as-synthesized samples were calcined at 550 °C for 6 h with an increasing temperature rate of 0.75 °C per minute. The samples are labeled "OSDA- x - y ". "OSDA" is the abbreviations of the templates used for the samples, including CTAB, $C_{18}N$, $C_{22}N$, $C_{18}N_2$, and $C_{22}N_2$. " x " and " y " mean the reaction time (days) of 100 and 150 °C, respectively. Without specification, all the samples for characterizations were after-calcination samples.

The samples containing aluminum were synthesized by the same method, using aluminum sulfate octadecahydrate as the aluminum source, with different ratios of Si/Al. These samples were used for catalytic reaction.

Catalytic Reaction. The catalytic performance of as-synthesized samples was compared with conventional MCM-41 materials and ZSM-5 at different ratios of Si/Al.² All the materials were treated with ammonium acetate (1 M) aqueous solution stirred at 90 °C for ion exchange every 6 h three times. After the ion exchange, the samples were washed repeatedly with DI water and dried at 50 °C overnight. The materials were converted to H^+ form through calcination at 550 °C in air for 6 h. Before the catalytic reaction, the catalysts described above were preactivated at 150 °C for at least 2 h.

The catalytic experiments were carried out in heat-resistant glass bottle under N_2 atmosphere. The reaction was carried out at liquid phase and reaction mixtures, 2-hydroxyacetophenone (0.136 g, 1 mmol), benzaldehyde (0.159 g, 1.5 mmol), 0.5 mL DMF solvent, and 15 mg catalyst, were heated to 150 °C and stirred simultaneously for 14 h. The products were 2'-hydroxychalcone and flavanone. After the catalytic reaction, the samples were analyzed by High Performance Liquid Chromatography (HPLC) to determine the selectivity and conversion rate.

Characterization. Scanning electron microscopy (SEM) images were taken with a SU8010 field-emission scanning electron microscope operating at 3 kV. Power X-ray diffraction (PXRD) patterns were recorded in the 2θ range of 1–30° using $Cu K\alpha$ radiation (15 mA and 40 kV) with a step size of 0.012° and dwell time of 0.4 s at room temperature in a D/MAX-2500 rotating-anode X-ray diffractometer. Transmission electron microscopy (TEM) images were taken by a JEM-2100F transmission electron microscopy operated at an accelerating voltage of 200 kV. A drop of the dispersion was supported on a copper grid with holey carbon and then dried, prior to TEM characterization. Fourier-transform infrared (FT-TR) spectra were

carried out using the attenuated total reflectance method on Nicolet 6700 by Thermo Scientific. The spectrum was generated, collected 16 times, and corrected for the background noise. The experiments were done on the powdered samples with KBr addition. ^{29}Si MAS NMR spectra were tested with Infinityplus 300 of Varian. Nitrogen adsorption and desorption isotherms were measured at $-196\text{ }^\circ\text{C}$ on 3H-2000PM2 volumetric adsorption apparatus. Prior to each measurement, about 0.2 g of product was outgassed at $260\text{ }^\circ\text{C}$ to vacuum (-0.1 MPa). The elemental compositions of Si and Al were analyzed by inductively coupled plasma optical emission spectroscopy (ICP-OES) using a Horiba Ultima 2 instrument equipped with photomultiplier tube detection. 0.01 g of samples was dissolved in HF (40%, 3 mL) at room temperature for 30 min, diluted with saturated boric acid solution (45 mL).

The catalytic products were analyzed using LC3000 High Performance Liquid Chromatography (HPLC) system equipped with an ultraviolet detector at 215 nm. The system used a Kromasil 100-5C18 ($250 \times 4.6\text{ mm}$) column with 85% methanol and 15% water as mobile phase and the mobile phase flow rate was 1 mL/min. The sample injection size of 10 μL was used for detection.

3. RESULTS AND DISCUSSION

Figure 1A shows the XRD patterns of the samples reacting for 3 days at $100\text{ }^\circ\text{C}$. Three peaks were observed in low angle ($2\theta <$

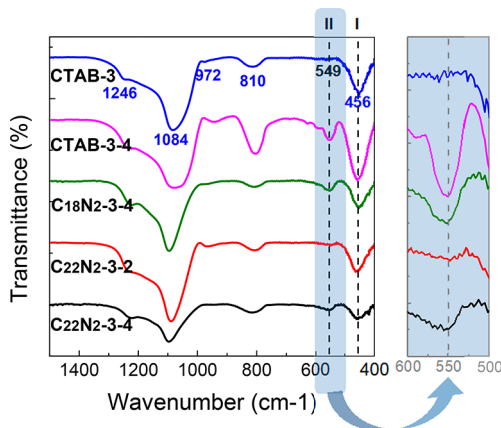


Figure 2. FT-IR patterns of some samples.

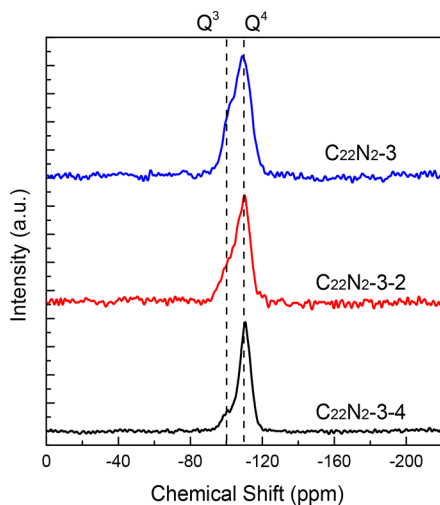


Figure 3. ^{29}Si MAS NMR of samples with C_{22}N_2 .

5°) in CTAB-3, C_{22}N_2 -3, and C_{18}N_2 -3, which could be indexed to the (100), (110), and (200) crystal faces of MCM-41. Only one peak was observed in C_{18}N -3, two peaks were observed in

C_{22}N -3. These two peaks could be assigned to (100) and (200) reflections of the lamellar M41s,^{26,27} and they disappeared after calcination. So, in this condition, CTAB-3, C_{18}N_2 -3, and C_{22}N_2 -3 formed MCM-41 structure, and the other two formed lamellar M41s.

When reacting 3 days at $100\text{ }^\circ\text{C}$ and then 2 days at $150\text{ }^\circ\text{C}$, from the low angle of XRD, order degrees of the mesoporous structure were reduced in CTAB-3-2, C_{18}N_2 -3-2, and C_{22}N_2 -3-2. C_{22}N -3-2 was still lamellar M41s with two peaks, which disappeared after calcination. However, C_{18}N -3-2 transformed to short-range ordered MCM-41, for (100) reflection was retained after calcination.^{28,29} Their XRD patterns are shown in Figure 1B. Compared with the XRD patterns of multilamellar MFI³⁰ and MCM-41 (PDF#49-1712), where the d -spacing of 100 face was 6.50 and 4.12 nm, respectively, the d -spacing_[100] of OSDA-3-2 was between 4.40 and 6.61 nm and is consistent with the literature report suggesting the transformation process from MCM-41 to silicalite-1 (Table S1). From high angle, two silicalite-1 peaks ($2\theta = 8.08^\circ$ and 9.04°) occurred in C_{22}N_2 -3-2 which were attributed to (101) and (020) crystal faces of silicalite-1 zeolite structure, indicating the partially crystallized MFI structure after temperature-gradient treatment. Figure 1C shows XRD patterns of samples reacting for 3 days at $100\text{ }^\circ\text{C}$, then 4 days at $150\text{ }^\circ\text{C}$. In low angle, CTAB-3-4 and C_{18}N -3-4 still retained the structure of MCM-41, and the d -spacing of 100 crystal face was 4.96 and 6.27 nm, respectively (Table S1). C_{22}N -3-4 remained lamellar M41s. Meanwhile, CTAB-3-4, C_{18}N_2 -3-4, and C_{22}N_2 -3-4 formed the silicalite-1 zeolite structure in high angle (at least four peaks in $2\theta = \sim 8^\circ$, $\sim 9^\circ$, $\sim 23^\circ$, and $\sim 24^\circ$), while the MCM-41 peaks of the latter two broke down after calcination. So C_{22}N_2 -3-2 and CTAB-3-4 are mixtures of microporous zeolite silicalite-1 and mesoporous material MCM-41.

The zeolite framework can be identified by FT-IR patterns. As shown in Figure 2 and Figure S1, the characteristic peaks of amorphous silica were marked in blue. The peak in 549 cm^{-1} marked in black was related to crystal zeolite according to reported data^{14,31,32} which were used to determine the crystalline degree of zeolites. The optical density ratio of peak II ($\sim 550\text{ cm}^{-1}$): peak I ($\sim 450\text{ cm}^{-1}$) is a probe to characterize the presence of a zeolite crystallized framework,³³ because amorphous silica does not show any absorption near 550 cm^{-1} . Peak II around 550 cm^{-1} appeared in CTAB-3-4, C_{18}N_2 -3-4, C_{22}N_2 -3-2, and C_{22}N_2 -3-4, so the extents of crystallization of these samples represented by optical density ratios of the two peaks were 0.54, 0.55, 0.40, and 0.60, respectively; the results were confirmed by wide-angle powder XRD patterns. The strong band sited in around 1084 cm^{-1} with a pronounced shoulder at 1246 cm^{-1} was corresponding T-O-T (T represents Si or Al) asymmetric stretching mode, while the weak peak around 810 cm^{-1} was assigned to the T-O-T symmetric stretching mode.³⁴

Figure 3 is the ^{29}Si MAS NMR of samples with C_{22}N_2 . Q^3 ($\delta = -100\text{ ppm}$) corresponds to $(\text{SiO})_3\text{Si-OH}$ deriving from the silanol groups on the zeolite surface,³⁵ and Q^4 ($\delta = -110\text{ ppm}$) corresponds to crystallographically nonequivalent sites $(\text{SiO})_4\text{Si}$. The ratio of Q^3 to Q^4 represents the degree of polymerization of silica framework.^{26,36} The Q^3/Q^4 values of MCM-41 and ZSM-5 reported by Chen et al.²⁶ are 0.62 and 0.05. For C_{22}N_2 -3, C_{22}N_2 -3-2, and C_{22}N_2 -3-4, they are 0.60, 0.40, and 0.19, respectively. It proved again that the degrees of crystallization of these three samples increased successively.

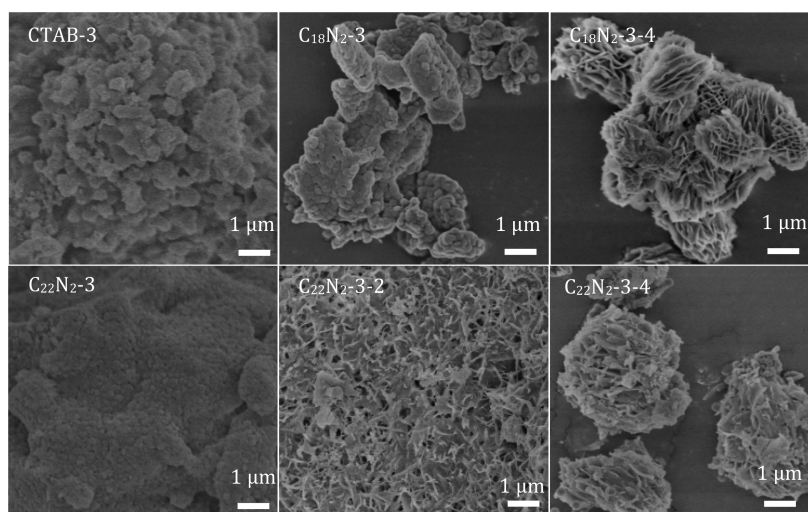


Figure 4. SEM images of some samples.

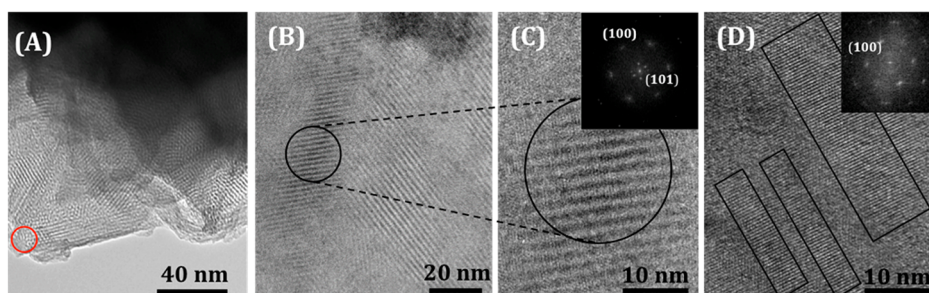


Figure 5. TEM images of $C_{22}N_2-3-2$, the inset pictures in C and D are fast Fourier transformation (FFT) of selected area.

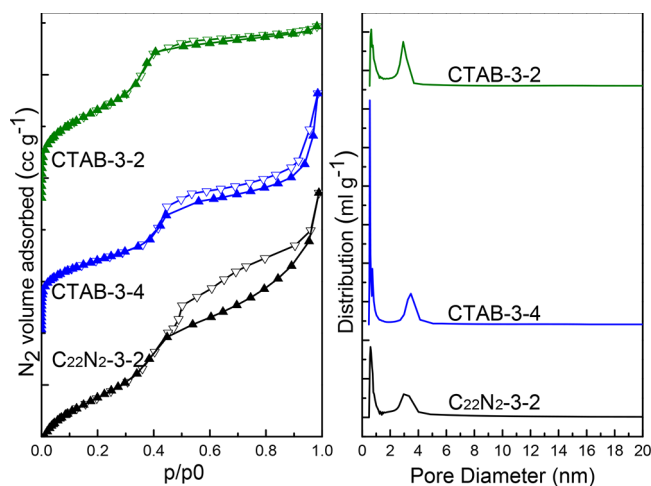


Figure 6. N_2 adsorption–desorption isotherms and pore size distributions of the micromesoporous composites.

SEM images of some samples were shown in Figure 4 with different morphologies. Other samples are in Figure S2. CTAB-3, $C_{18}N_2-3$, and $C_{22}N_2-3$ exhibit granular morphology with a granularity of about 0.4, 0.2, and 0.15 μm , respectively. $C_{18}N_2-3-4$ and $C_{22}N_2-3-4$ shows a lamellar morphology. $C_{22}N_2-3-2$ is an intermediate state between $C_{22}N_2-3$ and $C_{22}N_2-3-4$, showing some reticulated pieces. So does $C_{18}N_2-3-2$.

Figure 5 show the TEM images of $C_{22}N_2-3-2$. Other samples are in Figure S3. Samples with $C_{22}N_2$ and $C_{18}N_2$ show two-dimensional straight channels in the first and second

conditions, but in the third condition the structure disappeared because of the ruin of the mesoporous structure. On the contrary, for samples with $C_{18}N_2$, the channels appear in the two conditions with increased temperature but are absent from the first one. Some bending short channels are found in $C_{22}N_2-3-2$ and $C_{22}N_2-3-4$, showing disordered mesopores, which can be considered as the intermediate state during transformation between lamellar M41s and MCM-41,¹⁴ indicating the possibility of transformation to MCM-41.

More details about morphologies are shown in TEM images (Figure 5). Figure 5A shows the samples possessed channels of a hexagonal array in red circle, which were parallel direction of the hexagonal or cylindrical pores, the characteristic pores of MCM-41. Figure 5B shows the composite structure with some crystalline MFI centers distributed in long-range mesoporous materials. Samples directed by $C_{22}N_2$ formed MCM-41 at 100 $^{\circ}\text{C}$ and partly transformed to silicalite-1 at 150 $^{\circ}\text{C}$, so the ordered mesoporous material were broken by disperse silicalite-1 domain, becoming a composite of silicalite-1 and MCM-41. The calculated pore diameter of 4.23 nm from FFT pattern inserted in Figure 5C was corresponding with the (100) d -spacing of MCM-41. The pore diameter calculated from inner FFT pattern was 1.12 nm, which was attributed to the (101) crystal face of silicalite-1, where the d -spacing were around 1.10 nm.^{37,38} The good matched results demonstrate that the samples directed by $C_{22}N_2$ can simultaneously possess crystalline silicalite-1 zeolitic domains in mesoporous MCM-41 through controllable synthesis time. Figure 5D and the inserted FFT pattern illustrate silicalite-1 crystalline domains more specifically. This material has the advantages that the

Table 1. Textural Property Measured by N₂ Adsorption–Desorption Isotherm

	S_{BET} [m ² g ⁻¹]	S_{micro} [m ² g ⁻¹]	S_{ext} [m ² g ⁻¹]	V_{total} [cm ³ g ⁻¹]	V_{micro} [cm ³ g ⁻¹]	V_{meso} [cm ³ g ⁻¹]	d_p [nm]	d_w [nm]
CTAB-3	993	0	993	0.71	0	0.71	3.54	0.95
CTAB-3–2	662	13	649	0.53	0	0.53	4.09	0.99
CTAB-3–4	503	80	423	0.72	0.03	0.68	4.57	1.01
C ₁₈ N-3	446	0	446	0.30	0	0.30	^a	^a
C ₁₈ N-3–2	828	0	828	1.22	0	1.22	6.08	1.55
C ₁₈ N-3–4	674	0	674	0.94	0	0.94	5.68	1.56
C ₂₂ N-3	683	0	683	0.44	0	0.44	^a	^a
C ₂₂ N-3–2	581	0	581	0.47	0	0.47	^a	^a
C ₂₂ N-3–4	558	0	558	1.07	0	1.07	^a	^a
C ₁₈ N ₂ -3	936	0	936	0.52	0	0.52	2.58	1.66
C ₁₈ N ₂ -3–2	893	0	893	0.73	0	0.73	3.78	1.31
C ₁₈ N ₂ -3–4	306	143	164	0.46	0.07	0.40	^b	^c
C ₂₂ N ₂ -3	1268	0	1268	1.07	0	1.07	3.18	1.59
C ₂₂ N ₂ -3–2	1046	197	849	0.89	0.23	0.66	4.41	1.10
C ₂₂ N ₂ -3–4	288	160	128	0.55	0.08	0.47	^b	^c

^aNo MCM-41 structure. ^bNo uniform pore size distribution. ^cNo (100) crystal face was observed in XRD.

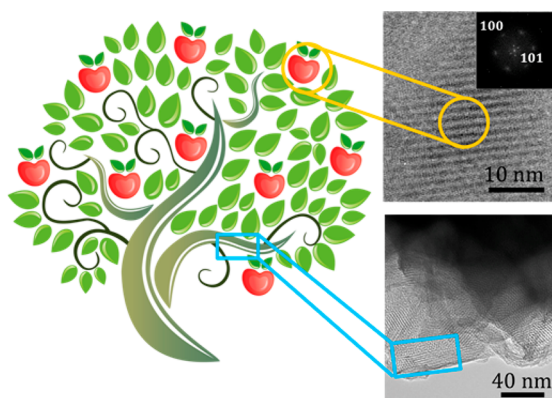


Figure 7. Illustration of the composite material.

mesopores provide good diffusibility and crystal microparticles can serve as catalytic sites. Figure 5D shows lattice fringes in one crystalline part of this sample.

N₂ adsorption–desorption isotherms were used to reveal the porosity features of MCM-41 samples. The isotherms generally belong to type-IV N₂ isotherms³⁹ with various hysteresis loops. The pore size distributions were derived from N₂ adsorption–desorption isotherms (BJH on the adsorption branch). Figure 6

and Figure S4 show N₂ adsorption–desorption isotherms and pore size distributions of some samples. Narrow dumbbell-shaped hysteresis loops appeared in CTAB-3, C₁₈N₂-3, and C₂₂N₂-3. One head of the “dumbbell” in the range of $P/P_0 = 0.45–0.74$ indicated the presence of mesopores within the materials. Another head in the range of $P/P_0 > 0.85$ can be attributed to the interparticle mesopores, and they have a narrow pore size distribution (pore size will be discussed in detail in the next sections). These results show that they have highly ordered MCM-41 structures. After undergoing a high temperature stage at 150 °C, their order degrees were found to decrease and pore sizes increase. Peaks in micropore area of about 0.55 nm appeared in CTAB-3–2, CTAB-3–4, and C₂₂N₂-3–2, indicating the formation of silicalite-1 zeolite phase while keeping the original mesoporous phase. The shape of the hysteresis loop of C₂₂N₂-3–2 is related to channel block of mesopores resulting from partial crystallization. In C₁₈N₂-3–4 and C₂₂N₂-3–4, micropores are obvious, but mesopores were destroyed.

C₁₈N-3 and C₂₂N-3 do not show obvious hysteresis loop, for their lamellar structures collapse after calcination. After a high temperature stage at 150 °C, type E hysteresis loops appear according to De Bore,⁴⁰ indicating formation of mesoporous structures. From the angle of pore size distributions, samples synthesized with C₁₈N have more uniform mesopores than

Table 2. Catalytic Data of Aldol Condensations Using Hierarchical Aluminosilicate Zeolites and Their Counterparts^a

Reaction ^[a]	Samples ^[b]	Conversion ratio ^[c]
 Flavanone Chalcone	Unilamellar MFI nanosheets (53) ^[d]	76 (64/32/5)
	MCM-41 (50) ^[e]	9 (58/42/0)
	Conventional MFI (41) ^[d]	16 (50/50/0)
	C ₂₂ N ₂ -3-2(49)	80(60/34/6)*

^a[a]HPLC trace of organics was provided in Figure S7. ^[b]The numbers in brackets represent the ratios of Si/Al. ^[c]The numbers in parentheses represent selectivity: (flavanone/chalcone/others). ^[d]The result obtained from Choi M et al.²² ^[e]The result obtained from Zhu. Y.⁴⁷. *The change of conversion was within 2.2% over three runs.

those with $C_{22}N$. This means that the extent of transformation from lamellar structure to MCM-41 are greater in samples with $C_{18}N$ than $C_{22}N$ in the same condition, in accordance with XRD results. It could be attributed to higher solubility in water of $C_{18}N$, and $C_{18}N$ is easier to form precursor micelles.

Table 1 lists the textural properties of samples determined from the N_2 adsorption–desorption isotherms. BET surface area (S_{BET}) was determined by multipoint BET method in a relative pressure range (P/P_0) of 0.05–0.20 of N_2 adsorption isotherm. Micropore volume (V_{micro}), micropore surface area (S_{micro}), and external surface area (S_{ext}) were determined by t -method. Total pore volume (V_{total}) was determined at $P/P_0 = 0.97$. Mesopore volume (V_{meso}) = $V_{total} - V_{micro}$. Pore size (d_p) was calculated by Nonlocal Density Functional Theory (NLDFT). Pore wall thickness (d_w) was calculated by a_0 (crystal lattice parameter) minus d_p . $a_0 = 2d_{(100)}/3^{1/2}$, $d_{(100)}$ was derived from XRD data.

In general, MCM-41 has a specific surface area of about 1000 m^2/g . CTAB-3 is 993 m^2/g and consistent with it. $C_{18}N_2-3$ is 936 m^2/g and $C_{22}N_2-3$ has a larger specific surface area of 1268 m^2/g . Another batch of sample $C_{22}N_2-3$ even shows a BET surface area as high as 2000 m^2/g (Figure S5). This extremely high BET surface area might indicate the formation trend of the mixture structure of microporous zeolite and mesoporous material. It is generally believed to be difficult to prepare good MCM-41 with long-chain (more than 22 C) surfactants.⁴¹ However, we find that $C_{22}N_2$, a long-chain surfactant with 34 main chain carbon, can form good MCM-41 structure. Their corresponding single quaternary ammonium salts $C_{22}N$ and $C_{18}N$ have the abilities to direct lamellar M41s at 100 °C and transform structures to MCM-41 at 150 °C, although no crystallization was observed in this condition. The OSDA $C_{22}N_2$, $C_{18}N_2$, $C_{22}N$, and $C_{18}N$, if counted by the carbon number of main chain, are 34, 30, 28, and 24, respectively. To the best of our knowledge, these quaternary ammonium salts are templates with the longest carbon chain ever used to direct a mesoporous structure.

After treatment at 150 °C, specific surface areas of CTAB-3–2, CTAB-3–4, $C_{18}N_2-3-2$, and $C_{22}N_2-3-2$ reduced to 662, 503, 893, and 1046 m^2/g , indicating partial collapse of the mesoporous structure along with the beginning of crystallization. $C_{18}N_2-3-4$ and $C_{22}N_2-3-4$ have really small specific surface areas of 306 and 288 m^2/g , because of the collapse of their mesoporous structure and formation of layered structure with higher aspect ratio. Their pore volumes also show a decreased trend along with the crystallization. For $C_{18}N$ and $C_{22}N$, however, different results are observed. $C_{18}N-3$ has a small specific surface area of 446 m^2/g and a low pore volume of 0.30 cm^3/g . After treatment at 150 °C, they increase to 828 m^2/g and 1.22 cm^3/g in $C_{18}N-3-2$ and slightly reduce in $C_{18}N-3-4$. These results prove again that the structure (lamellar M41s) of $C_{18}N-3$ is easy to transform to a more stable structure (MCM-41) in $C_{18}N-3-2$ and $C_{18}N-3-4$ at high temperature. Samples with $C_{22}N$ have small specific surface areas and pore volumes except for the pore volume of $C_{22}N-3-4$ (1.07 cm^3/g). If the reaction time was prolonged at 150 °C, it could be transformed to an MCM-41 structure. Among all the samples, CTAB-3–2, CTAB-3–4, $C_{18}N_2-3-4$, $C_{22}N_2-3-2$, and $C_{22}N_2-3-4$ have a certain proportion of micropores, which means they are partially or fully crystallized. $C_{22}N_2-3-2$ exhibited a BET surface of 1046 m^2/g , while the surface and volume of micropore is 197 m^2/g and 0.23 cm^3g^{-1} , respectively, which demonstrates good potential in the field of catalysis somehow.

Pore size and pore wall thickness are also our interests. These two values of CTAB-3 are 3.54 and 0.95 nm respectively and in accordance with 3.8 and 1.0 nm of reported data.²⁵ For $C_{18}N_2-3$ and $C_{22}N_2-3$, their pore sizes are smaller (2.58 and 3.18 nm) but pore walls are thicker (1.66 and 1.59 nm) because of the long headgroup of two C6 chains. The pore size increased and pore wall thickness decreased after treatment at 150 °C. Because the pore wall thickness of ordinary MCM-41 is about 1 nm,² a single unit cell dimension along the b -axis of silicalite-1 is about 2 nm.²² So the thicker pore walls will be beneficial to the formation of crystallized structure. In this sense $C_{18}N_2$ and $C_{22}N_2$ are apparently better than CTAB in preparing this kind of material.

As we can see, single and gemini quaternary ammonium salts direct to different structures in 100 °C. This can be explained by their different packing parameters. Packing parameter of a surfactant can be expressed as $g = V/a_0l$, in which V is the volume of the surfactant chain, a_0 is effective area of the head, and l is effective length of the tail. The surfactant easily directs to hexagonal phase when $g = 0.5$, and to lamellar phase when $g = 1$.²⁴ For long chain surfactants, their l is short because of the bending of the long tail, so their g value is large.⁴² That is why very-long-chain surfactants are difficult to direct to good MCM-41 in general opinion. As results showed, $C_{18}N$ and $C_{22}N$ could direct to lamellar phase at 100 °C, and then they would transform structure into hexagonal phase in 150 °C via the mechanism reported by Monnier et al.⁴³ For $C_{18}N_2$ and $C_{22}N_2$ however, their a_0 is almost two times that of $C_{18}N$ and $C_{22}N$ because of the large headgroup.⁴⁴ So their g values are much smaller than $C_{18}N$ and $C_{22}N$, and easily direct to hexagonal phase, although they have the same tail.

Taking into consideration the above characterizations, we provide a possible “apple-tree highway” transportation mechanism for illustrating the potential advantage of as-synthesized samples (Figure 7). The crystalline silicalite-1 distributes in the big mesoporous area in a highly dispersed way. Distributed small crystalline areas, just like apples in the tree, serving as catalytic sites, while mesoporous “branches” of the tree are highways for transporting cargoes because of the good diffusibility of mesopores. This kind of material is expected to have high catalytic performance as well as high transmission efficiency of reactants and products, which is a promising material in acid catalysis.

For demonstrating the “apple-tree highway” mechanism, we prepared hierarchical aluminosilicate zeolites with $C_{22}N_2$ serving as surfactant. The relative characterizations were shown in Supporting Information (Figure S6). For catalytic tests, 2-hydroxychalcone and flavanone, members of chalconoids and flavonoids families, respectively, were usually obtained by Claisen-Schmidt condensation of benzaldehyde with 2'-hydroxyacetophenone and subsequent isomerization.^{45,46} Solid catalysts were important in heterogenous catalysis due to the easiness of separation and recovery. In our experiments, the $C_{22}N_2-3-2$ with special ratio of Si/Al is used as catalyst for the Claisen-Schmidt condensation of benzaldehyde with 2'-hydroxyacetophenone reaction. The catalytic performances of the hierarchical composite, the conventional MCM-41 zeolite, and ZSM-5 are listed in Table 2. The conversion of 2'-hydroxyacetophenone under $C_{22}N_2-3-2$ (49) reaches 80%, which surpasses the activity of unilamellar MFI (76%), while the selectivity of flavanone is also similar. We also recycled the $C_{22}N_2-3-2$ (49) in the aldol condensation reaction three times and the change of conversion rate was within 2.2%.

The inferior catalytic performance of conventional MCM-41 and ZSM-5 was attributed to the fewer acid sites and low efficiency of diffusion, respectively. The hierarchical composites provide an enhancing catalytic activity in aldol condensation through combining the advantages of mesoporosity and MFI framework acidity.

4. CONCLUSIONS

In summary, we have demonstrated a single-template strategy to synthesize a hierarchical composite material, with a temperature-raising method. Meanwhile, the two-section temperature-gradient strategy was developed to balance the inherent compromise between the zeolitic and mesoporous structure, in which mesoporous structure was first introduced at lower temperature and zeolite framework was formed at higher temperature. Gemini quaternary ammonium salt surfactants such as $C_{22}N_2$ display better abilities in directing the structure of MCM-41 than CTAB at 100 °C and will gradually crystallize samples to lamellar silicalite-1 structures at 150 °C. It is possible to get a composite of microporous and mesoporous material by control the reaction time. Though inducing acid sites, the hierarchical composite exhibit outstanding catalytic activity in aldol condensation of bulky reactants, providing a valuable catalyst for a wide-range of applications.

■ ASSOCIATED CONTENT

Supporting Information

The Supporting Information is available free of charge on the ACS Publications website at DOI: [10.1021/acs.cgd.7b01649](https://doi.org/10.1021/acs.cgd.7b01649).

Experimental procedure and characterization data (PDF)

■ AUTHOR INFORMATION

Corresponding Author

*E-mail: guoxh@tju.edu.cn.

ORCID

He Ding: [0000-0002-2056-4618](https://orcid.org/0000-0002-2056-4618)

Xianghai Guo: [0000-0002-1519-4050](https://orcid.org/0000-0002-1519-4050)

Author Contributions

[#]He Ding and Yixiao Zhang contributed equally to this work.

Notes

The authors declare no competing financial interest.

■ ACKNOWLEDGMENTS

We gratefully acknowledge the funding for this work provided by the National Natural Science Foundation of China (No. 21202116), Independent Innovation Foundation of Tianjin University of China (No. 2017XZY-0052), and Natural Science Foundation of Tianjin of China (No. 16JCYBJC20300). Part of this work began at University of Minnesota, we are grateful to professor Michael Tsapatsis for his support and instructive discussion. We also want to thank Dr. Limin Ren for her supportive advices.

■ REFERENCES

- (1) Beck, J. S.; Vartuli, J. C.; Roth, W. J.; Leonowicz, M. E.; Kresge, C. T.; Schmitt, K. D.; Chu, C. T. W.; Olson, D. H.; Sheppard, E. W.; et al. A new family of mesoporous molecular sieves prepared with liquid crystal templates. *J. Am. Chem. Soc.* **1992**, *114* (27), 10834–43.
- (2) Kresge, C. T.; Leonowicz, M. E.; Roth, W. J.; Vartuli, J. C.; Beck, J. S. Ordered mesoporous molecular sieves synthesized by a liquid-crystal template mechanism. *Nature* **1992**, *359* (6397), 710–712.
- (3) Kresge, C. T.; Roth, W. J. The discovery of mesoporous molecular sieves from the twenty year perspective. *Chem. Soc. Rev.* **2013**, *42* (9), 3663.
- (4) Zhao, X. S.; Lu, G. Q.; Whittaker, A. K.; Millar, G. J.; Zhu, H. Y. Comprehensive Study of Surface Chemistry of MCM-41 Using ^{29}Si CP/MAS NMR, FTIR, Pyridine-TPD, and TGA. *J. Phys. Chem. B* **1997**, *101* (33), 6525–6531.
- (5) Corma, A. From Microporous to Mesoporous Molecular Sieve Materials and Their Use in Catalysis. *Chem. Rev. (Washington, DC, U. S.)* **1997**, *97* (6), 2373–2419.
- (6) Schmidt-Winkel, P.; Lukens, W. W.; Yang, P.; Margolese, D. I.; Lettow, J. S.; Ying, J. Y.; Stucky, G. D. Microemulsion Templating of Siliceous Mesostructured Cellular Foams with Well-Defined Ultralarge Mesopores. *Chem. Mater.* **2000**, *12* (3), 686–696.
- (7) Maschmeyer, T.; Rey, F.; Sankar, G.; Thomas, J. M. Heterogeneous catalysts obtained by grafting metallocene complexes onto mesoporous silica. *Nature* **1995**, *378* (6553), 159–162.
- (8) Shephard, D. S.; Maschmeyer, T.; Johnson, B. F. G.; Thomas, J. M.; Sankar, G.; Ozkaya, D.; Zhou, W.; Oldroyd, R. D.; Bell, R. G. Bimetallic Nanoparticle Catalysts Anchored Inside Mesoporous Silica. *Angew. Chem., Int. Ed. Engl.* **1997**, *36* (20), 2242–2245.
- (9) Van Looveren, L. K.; Geysen, D. F.; Vercruysee, K. A.; Wouters, B. H.; Grobet, P. J.; Jacobs, P. A. Methylalumoxane MCM-41 as Support in the Co-Oligomerization of Ethene and Propene with $[C_2H_4(1\text{-indenyl})_2]Zr(CH_3)_2$. *Angew. Chem., Int. Ed.* **1998**, *37* (4), 517–520.
- (10) Kim, J. M.; Jun, S.; Ryoo, R. Improvement of Hydrothermal Stability of Mesoporous Silica Using Salts: Reinvestigation for Time-Dependent Effects. *J. Phys. Chem. B* **1999**, *103* (30), 6200–6205.
- (11) Mokaya, R. Ultrastable Mesoporous Aluminosilicates by Grafting Routes. *Angew. Chem., Int. Ed.* **1999**, *38* (19), 2930–2934.
- (12) Corma, A.; Grande, M. S.; Gonzalez-Alfaro, V.; Orchilles, A. V. Cracking Activity and Hydrothermal Stability of MCM-41 and Its Comparison with Amorphous Silica-Alumina and a USY Zeolite. *J. Catal.* **1996**, *159* (2), 375–382.
- (13) Karlsson, A.; Stöcker, M.; Schmidt, R. Composites of micro- and mesoporous materials: simultaneous syntheses of MFI/MCM-41 like phases by a mixed template approach. *Microporous Mesoporous Mater.* **1999**, *27* (2–3), 181–192.
- (14) Huang, L.; Guo, W.; Deng, P.; Xue, Z.; Li, Q. Investigation of Synthesizing MCM-41/ZSM-5 Composites. *J. Phys. Chem. B* **2000**, *104* (13), 2817–2823.
- (15) Mavrodinova, V.; Popova, M.; Valchev, V.; Nickolov, R.; Minchev, C. Beta zeolite colloidal nanocrystals supported on mesoporous MCM-41. *J. Colloid Interface Sci.* **2005**, *286* (1), 268–273.
- (16) Zhang, H.; Meng, X.; Li, Y.; Lin, Y. S. MCM-41 Overgrown on Y Composite Zeolite as Support of Pd–Pt Catalyst for Hydrogenation of Polyaromatic Compounds. *Ind. Eng. Chem. Res.* **2007**, *46* (12), 4186–4192.
- (17) Zhang, H.; Li, Y. Preparation and characterization of Beta/MCM-41 composite zeolite with a stepwise-distributed pore structure. *Powder Technol.* **2008**, *183* (1), 73–78.
- (18) Yang, D.; Xu, Y.; Zhai, S.; Zheng, J.; Li, J.; Wu, D.; Sun, Y. Facile Nonsurfactant Route to Silica-based Bimodal Xerogels with Micro/Mesopores. *Chem. Lett.* **2005**, *34* (8), 1138–1139.
- (19) Liu, Y.; Zhang, W.; Pinnavaia, T. J. Steam-Stable Aluminosilicate Mesostructures Assembled from Zeolite Type Y Seeds. *J. Am. Chem. Soc.* **2000**, *122* (36), 8791–8792.
- (20) Liu, Y.; Pinnavaia, T. J. Aluminosilicate mesostructures with improved acidity and hydrothermal stability. *J. Mater. Chem.* **2002**, *12* (11), 3179–3190.
- (21) Xia, Y.; Mokaya, R. Are mesoporous silicas and aluminosilicas assembled from zeolite seeds inherently hydrothermally stable? Comparative evaluation of MCM-48 materials assembled from zeolite seeds. *J. Mater. Chem.* **2004**, *14* (23), 3427.
- (22) Choi, M.; Na, K.; Kim, J.; Sakamoto, Y.; Terasaki, O.; Ryoo, R. Stable single-unit-cell nanosheets of zeolite MFI as active and long-lived catalysts. *Nature* **2009**, *461* (7261), 246–249.

- (23) Na, K.; Jo, C.; Kim, J.; Cho, K.; Jung, J.; Seo, Y.; Messinger, R. J.; Chmelka, B. F.; Ryoo, R. Directing Zeolite Structures into Hierarchically Nanoporous Architectures. *Science* **2011**, *333*, 328–332.
- (24) Huo, Q.; Margolese, D. I.; Stucky, G. D. Surfactant Control of Phases in the Synthesis of Mesoporous Silica-Based Materials. *Chem. Mater.* **1996**, *8* (5), 1147–60.
- (25) Zhao, D.; Wan, Y.; Zhou, W. *Ordered Mesoporous Molecular Sieve Materials*; Higher Education Press, 2013; pp 165–171.
- (26) Chen, X.; Huang, L.; Li, Q. Hydrothermal Transformation and Characterization of Porous Silica Templated by Surfactants. *J. Phys. Chem. B* **1997**, *101* (42), 8460–8467.
- (27) Vartuli, J. C.; Schmitt, K. D.; Kresge, C. T.; Roth, W. J.; Leonowicz, M. E.; McCullen, S. B.; Hellring, S. D.; Beck, J. S.; Schlenker, J. L. Effect of Surfactant/Silica Molar Ratios on the Formation of Mesoporous Molecular Sieves: Inorganic Mimicry of Surfactant Liquid-Crystal Phases and Mechanistic Implications. *Chem. Mater.* **1994**, *6* (12), 2317–2326.
- (28) Tanev, P. T.; Chibwe, M.; Pinnavaia, T. J. Titanium-containing mesoporous molecular sieves for catalytic oxidation of aromatic compounds. *Nature* **1994**, *368* (6469), 321–323.
- (29) Tanev, P. T.; Pinnavaia, T. J. A Neutral Templating Route to Mesoporous Molecular Sieves. *Science* **1995**, *267* (5199), 865.
- (30) Park, W.; Yu, D.; Na, K.; Jelfs, K.; Slater, B.; Sakamoto, Y.; Ryoo, R. Hierarchically Structure-Directing Effect of Multi-Ammonium Surfactants for the Generation of MFI Zeolite Nanosheets. *Chem. Mater.* **2011**, *23*, 5131.
- (31) Chen, C.-Y.; Li, H.-X.; Davis, M. E. Studies on mesoporous materials I. Synthesis and characterization of MCM-41. *Microporous Mater.* **1993**, *2* (1), 17–26.
- (32) Yu, J.; Li, M.; Tian, Y.; Ma, X.; Li, Y. Effect of Si/Al ratio and a secondary hydrothermal treatment on the properties of Al-MSU-SFAU. *J. Porous Mater.* **2013**, *20* (5), 1387–1393.
- (33) Coudurier, G.; Naccache, C.; Vedrine, J. C. Uses of IR spectroscopy in identifying ZSM zeolite structure. *J. Chem. Soc., Chem. Commun.* **1982**, *24*, 1413–14.
- (34) Sang, Y.; Jiao, Q.; Li, H.; Wu, Q.; Zhao, Y.; Sun, K. HZSM-5/MCM-41 composite molecular sieves for the catalytic cracking of endothermic hydrocarbon fuels: nano-ZSM-5 zeolites as the source. *J. Nanopart. Res.* **2014**, *16* (12), 1 DOI: 10.1007/s11051-014-2755-x.
- (35) Maheshwari, S.; Martinez, C.; Teresa Portilla, M.; Llopis, F. J.; Corma, A.; Tsapatsis, M. Influence of layer structure preservation on the catalytic properties of the pillared zeolite MCM-36. *J. Catal.* **2010**, *272* (2), 298–308.
- (36) Xu, M.; Arnold, A.; Buchholz, A.; Wang, W.; Hunger, M. Low-Temperature Modification of Mesoporous MCM-41 Material with Sublimated Aluminum Chloride in Vacuum. *J. Phys. Chem. B* **2002**, *106* (47), 12140–12143.
- (37) Diaz, I.; Kokkoli, E.; Terasaki, O.; Tsapatsis, M. Surface Structure of Zeolite (MFI) Crystals. *Chem. Mater.* **2004**, *16* (25), 5226–5232.
- (38) Kim, W.-g.; Zhang, X.; Lee, J. S.; Tsapatsis, M.; Nair, S. Epitaxially Grown Layered MFI-Bulk MFI Hybrid Zeolitic Materials. *ACS Nano* **2012**, *6* (11), 9978–9988.
- (39) Gregg, S. J.; Sing, K. S. W. *Adsorption, Surface Area and Porosity*, 2nd ed.; Academic Press, 1982.
- (40) Everett, D. H.; Stone, F. S. *The Structure and Properties of Porous Materials*; Butterworth: London, 1958.
- (41) Kruk, M.; Jaroniec, M.; Sakamoto, Y.; Terasaki, O.; Ryoo, R.; Ko, C. H. Determination of pore size and pore wall structure of MCM-41 by nitrogen adsorption, transmission electron microscopy, and x-ray diffraction. *J. Phys. Chem. B* **2000**, *104* (2), 292–301.
- (42) Rosen, M. J.; Kunjappu, J. T. *Micelle Formation by Surfactants, in Surfactants and Interfacial Phenomena*, 4th ed.; John Wiley & Sons, Inc.: Hoboken, NJ, 2012; pp 123–201.
- (43) Monnier, A.; Schüth, F.; Huo, Q.; Kumar, D.; Margolese, D.; Maxwell, R. S.; Stucky, G. D.; Krishnamurty, M.; Petroff, P.; Firouzi, A.; Janicke, M.; Chmelka, B. F. Cooperative Formation of Inorganic-Organic Interfaces in the Synthesis of Silicate Mesostructures. *Science* **1993**, *261* (5126), 1299.
- (44) Israelachvili, J. N.; Mitchell, D. J.; Ninham, B. W. Theory of self-assembly of hydrocarbon amphiphiles into micelles and bilayers. *J. Chem. Soc., Faraday Trans. 2* **1976**, *72* (0), 1525–1568.
- (45) Nath Dhar, D. *The Chemistry of Chalcones and Related Compounds*; John Wiley and Sons, 1981.
- (46) *Plant flavonoids in biology and medicine. Biochemical, pharmacological, and structure-activity relationships*; Proceedings of a symposium; Buffalo, New York, July 22–26, 1985.
- (47) Zhu, Y.; Hua, Z.; Zhou, J.; Wang, L.; Zhao, J.; Gong, Y.; Wu, W.; Ruan, M.; Shi, J. Hierarchical Mesoporous Zeolites: Direct Self-Assembly Synthesis in a Conventional Surfactant Solution by Kinetic Control over the Zeolite Seed Formation. *Chem. - Eur. J.* **2011**, *17* (51), 14618–14627.